



Study of residual stresses in Ti-7Al using theory and experiments



K. Chatterjee^a, J.Y.P. Ko^b, J.T. Weiss^c, H.T. Philipp^c, J. Becker^{b,c}, P. Purohit^c, S.M. Gruner^{b,c,d}, A.J. Beaudoin^{a,b,*}

^a Mechanical Science and Engineering, University of Illinois, 1206 West Green Street, Urbana-Champaign, IL 61801, USA

^b Cornell High Energy Synchrotron Source (CHESS), Cornell University, Ithaca, NY 14853, USA

^c Laboratory of Atomic and Solid State Physics, Cornell University, Ithaca, NY 14853, USA

^d Kavli Institute for Nanoscale Science, Cornell University, Ithaca, NY 14853, USA

ARTICLE INFO

Article history:

Received 6 April 2017

Revised 21 July 2017

Accepted 22 August 2017

Available online 24 August 2017

Keywords:

Ti-7Al alloy

Phenomenological mesoscopic field dislocation mechanics

High energy X-ray diffraction

Residual stress

Subgrain level stress

Strain rate sensitivity

ABSTRACT

Finite element simulations are carried out to follow the evolution of residual stresses in Ti-7Al (α -hcp) alloy, as developed under an applied stress gradient. A model built upon phenomenological mesoscopic field dislocation mechanics is employed to simulate the deformation behavior. Model predictions are validated with results generated from high energy X-ray diffraction experiments using synchrotron radiation. These experiments provide for important simulation input, viz. grain positions and orientations, and strain rate sensitivities of the prismatic and basal slip systems of Ti-7Al. X-ray diffraction data obtained from individual grains enabled calculation of strain rate sensitivities of the prismatic and basal slip systems and the values are estimated as ~ 0.04 and ~ 0.02 respectively. Residual stresses at the length scale of individual grains and subgrains are successfully predicted and validated against experimental data. A key achievement of the present work is the measurement and simulation of residual stress gradients within individual grains. Conclusions from this work are that grains deform mainly via prismatic slip, and accurate characterization of rate-sensitivity is needed to model the development of grain-level residual stresses.

© 2017 Elsevier Ltd. All rights reserved.

1. Introduction

Deformation and internal stress distribution in polycrystalline materials depend upon material texture, interactions among neighboring grains and types of loading (viz. tension, bending). A coordination of theoretical investigations and experiments at the length scale of a single grain is often necessary to gain insight into the complex mechanical behavior of polycrystals. Our effort in this work is bringing together the state-of-the-art modeling and experimental capabilities to explore the grain-level deformation mechanisms and residual stress situation in a polycrystalline α -Ti-Al alloy.

Modeling of grain-level deformation requires careful characterization of defects and their interactions at microscale. Aligned with the interest of crystal plasticity simulations are a clear distinction between statistically stored dislocations (SSD) and geometrically necessary dislocations (GND) and their individual contributions towards distribution of deformation (Arsenlis and Parks, 1999; Ashby, 1970). Crystal-scale numerical models for Ti-Al alloys often focus on studying the α -hcp

* Corresponding author.

E-mail address: abeaudoi@illinois.edu (A.J. Beaudoin).

phase only in order to keep the modeling simple but still gather information, representative of both near- α and $\alpha + \beta$ alloys (Dunne et al., 2012; Dunne and Rugg, 2008; Dunne et al., 2007; Hasija et al., 2003; Rugg et al., 2007). Rate-dependent crystal plasticity based finite element (CPFE) formulations have been developed in Ref. (Hasija et al., 2003; Venkatramani et al., 2007; Wang et al., 2011) in order to understand the effect of material texture on deformation behavior of Ti-Al alloys. Evolution of geometrically necessary dislocation density was not included in these numerical models, although, it is primarily important for deformation characterization at the scale of individual grains. Particularly, the work of Wang et al. (2011) addresses these shortcomings in conventional CPFE method. Therefore, robust theoretical frameworks and nonlocal finite element methods have been developed to include the GND density evolution in study of dwell fatigue of α -Ti alloys (Dunne et al., 2012; Dunne and Rugg, 2008; Dunne et al., 2007; Rugg et al., 2007). A nonlocal finite element method is required to evaluate the spatial gradients that contribute towards evolution of GND density. Our approach in this work, is to apply a nonlocal modified field dislocation mechanics theory called reduced phenomenological mesoscopic field dislocation mechanics (RPMFDM) (Roy et al., 2006), that uses both SSDs and GNDs for defining the deformation state of a material. SSDs can act as a source of GNDs (therefore, residual stresses) through dislocation evolution equation. A rate sensitive crystal plasticity framework is necessary to aid the calculations of reduced phenomenological mesoscopic field dislocation mechanics.

In addition to the appropriate physical modeling, validation with suitable experimental data helps to improve the predictive capability of crystal-based theoretical models. Surface measurements (viz. Electron backscatter diffraction, Digital image correlation) are commonly implemented for the validation purposes (Dunne et al., 2012; Dunne and Rugg, 2008; Rugg et al., 2007; Wang et al., 2011), but, these measurements have limitations, because, the subsurface deformation characteristics are often different from the surface - due to triaxial stress state inside the bulk material. Therefore, validation of a crystal-scale model is inadequate unless we have access to grain-level experimental data obtained from the bulk of a material. Besides, these 2D surface measurements are also frequently used for initializing a microstructure for simulation input, however, representation of the true 3D microstructure is important for grain-level simulation studies. Thankfully, high energy X-ray diffraction (HEXD), using synchrotron radiation, has emerged as a powerful engineering tool that essentially fulfills these needs. This method allows one to extract reliable grain-level data, particularly, strain and stress tensor, crystallographic orientation and center of mass of each grain from the bulk of a polycrystalline sample (Beaudoin et al., 2012; Bernier et al., 2010; Chatterjee et al., 2016; Poulsen, 2004; Pagan et al., 2017; Wang et al., 2011). Recently, Beaudoin et al. (2012) and Messner et al. (2014) linked crystal-plasticity models with HEXD experiments to demonstrate local variations of stress triaxiality and its impact on delamination cracking in Al-Li alloys. Bernier et al. (2010) predicted the critical resolved shear stresses and Pagan et al. (2017) described the evolution of slip system strengths of a α -Ti-Al alloy through a combined effort of crystal plasticity simulations and HEXD experiments. Grain positions and orientations obtained from the experimental measurements enabled them to form a virtual polycrystal for simulation work (Bernier et al., 2010; Pagan et al., 2017). These research works motivate us to take advantage of these experiments for proper assessment of our numerical results and for generating a virtual 3D microstructure to be used in simulation. Our research goes an extra step from previous works and introduces first-hand comparisons of stress distributions inside individual grains i.e. at the scale of subgrains from experiments and simulations.

Ti-7Al alloy is selected as the candidate material for the current research. This material has a hcp structure and exhibits mechanical behavior similar to that of the α -phase of many technologically important $\alpha + \beta$ Ti-Al alloys (viz. Ti-6Al-4V). Ti-Al alloys suffer from substantial room temperature creep at stress levels lower than their macroscopic yield stress (Adenstedt, 1949; Odegard and Thompson, 1974). The creep deformation is severe in presence of notches or manufacturing defects that give rise to localized stress gradients (stress concentrations). Significant residual stresses can develop in that case which in turn influences the mechanical failure of a component. Therefore, it is important to study creep deformation and residual stress development in Ti-Al alloys under an applied stress gradient. Earlier research works have established that the strain rate sensitivity of the alloy is a major factor, responsible for significant room-temperature creep of the material (Odegard and Thompson, 1974). Interestingly, the strain rate sensitivities associated with different slip systems of this alloy may be different, further contributing to the anisotropic nature of deformation. Strain rate sensitivities of different slip systems of Ti-Al alloys have been quantified using single crystal experiments (Hasija et al., 2003) or micro-pillar compression tests inside individual grains of an aggregate (Jun et al., 2016). In reference Jun et al. (2016), a detailed slip trace analysis was conducted so as to provide indication of the active slip system. Zhang et al. (2016a); 2016b) combined crystal plasticity formulations with micropillar compression tests to describe markedly different strain rate sensitivities associated with prismatic and basal slip systems of the α phase of Ti-6Al-2Sn-4Zr-2Mo. HEXD measurements are useful for determining strain rate sensitivities of individual grains during bulk deformation. The estimated values can be tested with the rate-sensitive theoretical model used in the current work.

Taken together, the objectives of the current work are as follows:

- Employ a crystal-based finite-element model using reduced phenomenological mesoscopic field dislocation mechanics to simulate grain-by-grain residual stress development under stress gradient in a virtual polycrystal of Ti-7Al alloy. The virtual polycrystal is generated using the crystallographic orientations and relative positions of grains determined from high energy X-ray diffraction experiments. In addition, HEXD experiments are used to assess the grain-level residual stresses developed through application of stress gradient in the Ti-7Al sample. Interestingly, we were also able to characterize subgrain-level stresses from both experiments and simulations.

- Estimate strain rate sensitivities of prismatic and basal slip systems of Ti-7Al from stress relaxation tests with HEXD and use the estimated values as input in the modeling.
- Interpret the experimentally found residual stresses using simulated results and gain insight into the slip system activities in the material.

The HEXD-based stress gradient study of Ti-7Al has been reported in Ref Chatterjee et al. (2016). This earlier study was primarily focused on investigating grain-level deformation behavior and residual stresses for central cross-section of the sample. In the current work, the objective is to explore the mechanical deformation of grains in entire 3D diffraction volume. A line focused X-ray beam (beam height $\sim 2 \mu\text{m}$) was used in the experiment that was particularly important for scanning several sections inside individual grains in the sample (grain size $\sim 100 \mu\text{m}$). Thereby, it facilitated the characterization of mechanical response at the scale of subgrains. For Ti-7Al stress relaxation experiments, diffraction data was acquired with a fast-framing Mixed-Mode Pixel Array Detector (MM-PAD; see Section 3, Materials and methods), capable of capturing images at rates as high as 1 kHz. A method was introduced to initialize the GND distribution i.e. the residual stresses in the virtual polycrystal for the modeling. Initialization of residual stresses in study of polycrystal plasticity has been an interesting problem and has recently been addressed by other researchers (Pokharel and Lebensohn, 2017).

2. Model formulation

2.1. Reduced Phenomenological Mesoscopic Field Dislocation Mechanics (RPMFDM)

Field dislocation mechanics is the study of motion and evolution of dislocations under the action of stress/force (Acharya, 2001; Acharya et al., 2008). Dislocation motion depends upon the stress/force field created by dislocation-dislocation interactions and applied boundary conditions. Phenomenological Mesoscopic Field Dislocation Mechanics (PMFDM) is derived by averaging the equations of field dislocation mechanics over space and time (Roy et al., 2006; Varadhan, 2007). Further, with the assumption of sufficient smoothness of the field variables, a reduced version of PMFDM can be developed. This framework, called Reduced Phenomenological Mesoscopic Field Dislocation Mechanics (RPMFDM) (Roy et al., 2006; Varadhan, 2007) is used for the current work. In PMFDM and RPMFDM, dislocations are classified into geometrically necessary dislocations (GND) and statistically stored dislocations (SSD). SSDs contribute only to overall plastic flow and GNDs are responsible for both plastic flow and long-range stresses. Both SSDs and GNDs contribute to the increment of plastic distortion which is further used to calculate dislocation density evolution, elastic distortion and stresses. A comparison of back stress developed through the two approaches is outlined in Roy et al. (2006). Thus, this theory allows to quantify the permanent deformation and residual stresses developed in a material. The phenomenology is introduced with the use of crystal plasticity in calculation of terms relevant for evaluating dislocation evolution and slip plastic distortion rate. The governing equations of RPMFDM are described below for the case of infinitesimally small deformation.

The stress equilibrium (Eq. (1a)) and constitutive equations (Eq. (1b)) are fundamental to the theory. These equations, along with the relevant traction and displacement boundary conditions (Eqs. (1c) and (1d)), are used to solve for the stress σ and displacement \mathbf{u} fields.

$$\operatorname{div}\sigma = 0 \quad (1a)$$

$$\sigma = \mathbf{C}^e : \mathbf{U}^e \quad (1b)$$

$$\sigma \cdot \mathbf{n} = \bar{\mathbf{T}} \quad \text{on } S_t \quad (1c)$$

$$\mathbf{u} = \bar{\mathbf{u}} \quad \text{on } S_u \quad (1d)$$

In Eqs. (1c) and (1d), $\bar{\mathbf{T}}$ and $\bar{\mathbf{u}}$ are the prescribed traction and displacement conditions on surfaces S_t and S_u respectively.

For the small deformation condition, as is the case here, the total distortion grad \mathbf{u} can be expressed by additive decomposition i.e. as sum of elastic (\mathbf{U}^e) and plastic (\mathbf{U}^p) distortions. So, the elastic distortion (\mathbf{U}^e) can be derived as:

$$\mathbf{U}^e = \operatorname{grad}\mathbf{u} - \mathbf{U}^p \quad (2)$$

The evolution of GND density can be directly related to the rate of plastic distortion (Eq. (3a)) which in turn depends on the motion of both SSDs and GNDs (Eq. (3a)). Here, α , the dislocation density tensor is used to describe GND density.

$$\dot{\alpha} = -\operatorname{curl}\mathbf{U}^p = -\operatorname{curl}(\alpha \times \mathbf{V} + \mathbf{L}^p) \quad (3a)$$

$$\alpha(\mathbf{V} \cdot \mathbf{n}) = \bar{\mathbf{F}} \quad \text{on } S_i \quad (3b)$$

where \mathbf{V} is the dislocation velocity vector (calculation procedure of \mathbf{V} is described in Appendix A.1) and \mathbf{L}^p is the slip plastic distortion rate due to motion of SSDs. Calculation of \mathbf{L}^p follows from the crystal plasticity model introduced in Section 2.2. In Eq. (3b) $\bar{\mathbf{F}}$ denotes prescribed influx of dislocations at boundary S_i .

In the RPMFDM framework, SSDs contribute a source term, $-\operatorname{curl} \mathbf{L}^p$, towards the evolution of GND density, as is evident from the dislocation evolution equation (Eq. (3a)). As a side note, proper treatment of continuity of the plastic distortion is critical in cases where grain boundary morphology presents a significant constraint (Taupin et al., 2016). In the present setting, addressing the deformation of equiaxed grains, only smoothness necessary to compute $\operatorname{curl} \mathbf{U}^p$ within an element is achieved through RPMFDM (Roy et al., 2006).

2.2. Crystal plasticity

Crystal plasticity is used for determination of slip plastic distortion rate \mathbf{L}^p as follows:

$$\mathbf{L}^p = \sum_s \rho_m b v_s \mathbf{P}_s \quad (4)$$

where ρ_m is the mobile dislocation density, which is a constant for the current work, and b is the magnitude of the burgers vector. The Schmid tensor \mathbf{P}_s is calculated as a dyadic product of slip direction (\mathbf{b}_s) and slip plane normal (\mathbf{n}_s) for the s th slip system (Eq. (5)):

$$\mathbf{P}_s = \mathbf{b}_s \otimes \mathbf{n}_s \quad (5)$$

The dislocation velocity v_s in Eq. (4) is estimated using a power-law relation (Eq. (6a)) with resolved shear stress τ_s (Eq. (6b)).

$$v_s = v_0 \operatorname{sgn}(\tau_s) \left(\frac{|\tau_s|}{\tau_0} \right)^{\frac{1}{m}} \quad (6a)$$

$$\tau_s = \mathbf{P}_s : \boldsymbol{\sigma} \quad (6b)$$

where v_0 is the reference velocity, τ_0 is the critical resolved shear stress (CRSS) and m is the strain rate sensitivity of the s th slip system. Further discussion of the crystal plasticity formulation is provided in Appendix A.1.

3. Materials and methods

3.1. Experiment and data analysis

Samples were prepared from Ti-7Al material - extruded and annealed to produce grains of size $\approx 100\text{ }\mu\text{m}$.

Two distinct experiments provide the foundation for the present study. The first experiment provides a map of grain position, orientation and lattice strain used to instantiate and validate the model. This experiment is detailed in reference Chatterjee et al. (2016) and is briefly recounted here for completeness. The second experiment focuses on the kinetics of slip and enables the discrimination of rate sensitivity between slip systems.

The grain mapping experiment was conducted at beamline 1-ID-E of the Advanced Photon Source (APS) at Argonne National Laboratory. The setup inside the experimental hutch and the sample coordinate system are illustrated in Fig. 1a. The tensile specimen was prepared with $1.5\text{ mm} \times 1.5\text{ mm}$ square gage section and 4 mm gage length (Fig. 1b). The sample was held by collets, with the lower collet intentionally offset with respect to the centerline – so as to create an initial state of bending. The magnitude of the bending moment was estimated to be 105 N-mm ; the details of this calculation are given in Section 3.2.2. Tension was applied through a load frame to create a stress gradient varying from near zero stress to yield across the sample cross-section (Fig. 1c). The specimen was probed with a line focused X-ray beam of size $2\text{ mm (H)} \times 1.7\text{ }\mu\text{m (V)}$ (Shastri et al., 2007). In total 15 layers (in 0.56 mm range, in steps of $20\text{ }\mu\text{m}$), along the tensile direction, were scanned around the center of the sample gage section. The line focused beam allowed for measurement of several locations within the same grain from different layers – this led to the derivation of stress distributions inside individual grains. Diffraction images were collected on a mid-field detector and a far-field “hydra” detector, and used for position/orientation and lattice strain, respectively. Diffraction images were analyzed for all 15 layers using FABLE and GrainSpotter (Schmidt, 2014) software packages to find grain orientations. Strain tensor and centroid positions of each grain were calculated following the same procedure as developed in Ref. Chatterjee et al. (2016). Data analysis was performed for points A, B and C, marked on the load-displacement curve (Fig. 1c).

The second set of high-energy X-ray diffraction experiments were performed for derivation of strain rate sensitivity of the different slip systems of Ti-7Al (schematic of the setup is given in Fig. 2a). These experiments were conducted at Cornell High Energy Synchrotron Source – an incident X-ray beam of energy 42 keV and size $2\text{ mm (H)} \times 500\text{ }\mu\text{m (V)}$ was used. A tensile specimen of gage section $1\text{ mm} \times 1\text{ mm}$ and gage length 12 mm (Fig. 2b) was loaded in tension and held at constant displacement for stress relaxation (Fig. 2c shows stress relaxation behavior). Diffraction images were collected using a single-chip module of the mixed-mode pixel array detector (MM-PAD) mated to a CdTe sensor (Becker et al., 2017; 2016; Tate et al., 2017), allowing efficient 1 kHz acquisition of high-energy X-ray images. The MM-PAD single-chip module has 128×128 pixels with a pixel size of $150\text{ }\mu\text{m} \times 150\text{ }\mu\text{m}$ and an active area of $19.2\text{ mm} \times 19.2\text{ mm}$. Though the MM-PAD is

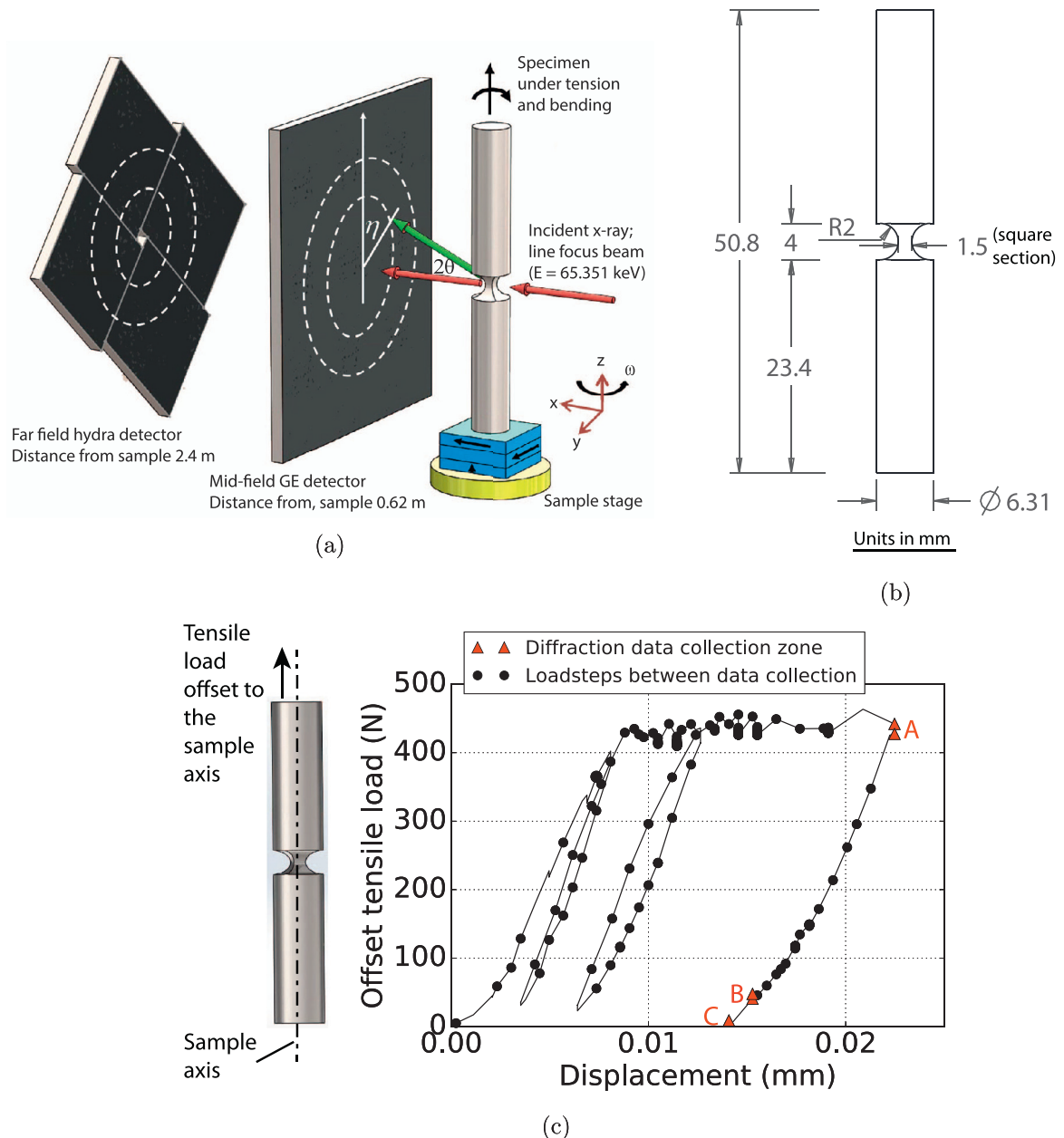


Fig. 1. (a) Schematic of the experimental setup at Advanced Photon Source, (b) The dimensions of the Ti-7Al sample used in the first set of experiments, (c) A tensile load, offset to the sample axis is applied to obtain a bending moment along with tension. Offset tensile load versus displacement plot for the specimen tested.

smaller than the GE detector, it enabled the examination of transients in isolated diffraction spots (Fig. 2d). The radial position shifts of a diffraction spot is directly proportional to the stress variations along the corresponding diffracting plane normal (also known as the diffraction vectors). Therefore, the stress relaxations along the plane normals and the associated rate sensitivities can be studied from the spot shifts vs. time data. Diffraction patterns obtained during each of the 5 relaxation periods (Fig. 2c) were used for the purpose of data analysis.

3.2. Simulation

A finite element analysis framework was developed that applies the theory of RPMFDM on a structured mesh geometry. The method of constructing the geometry is described in Section 3.2.1.

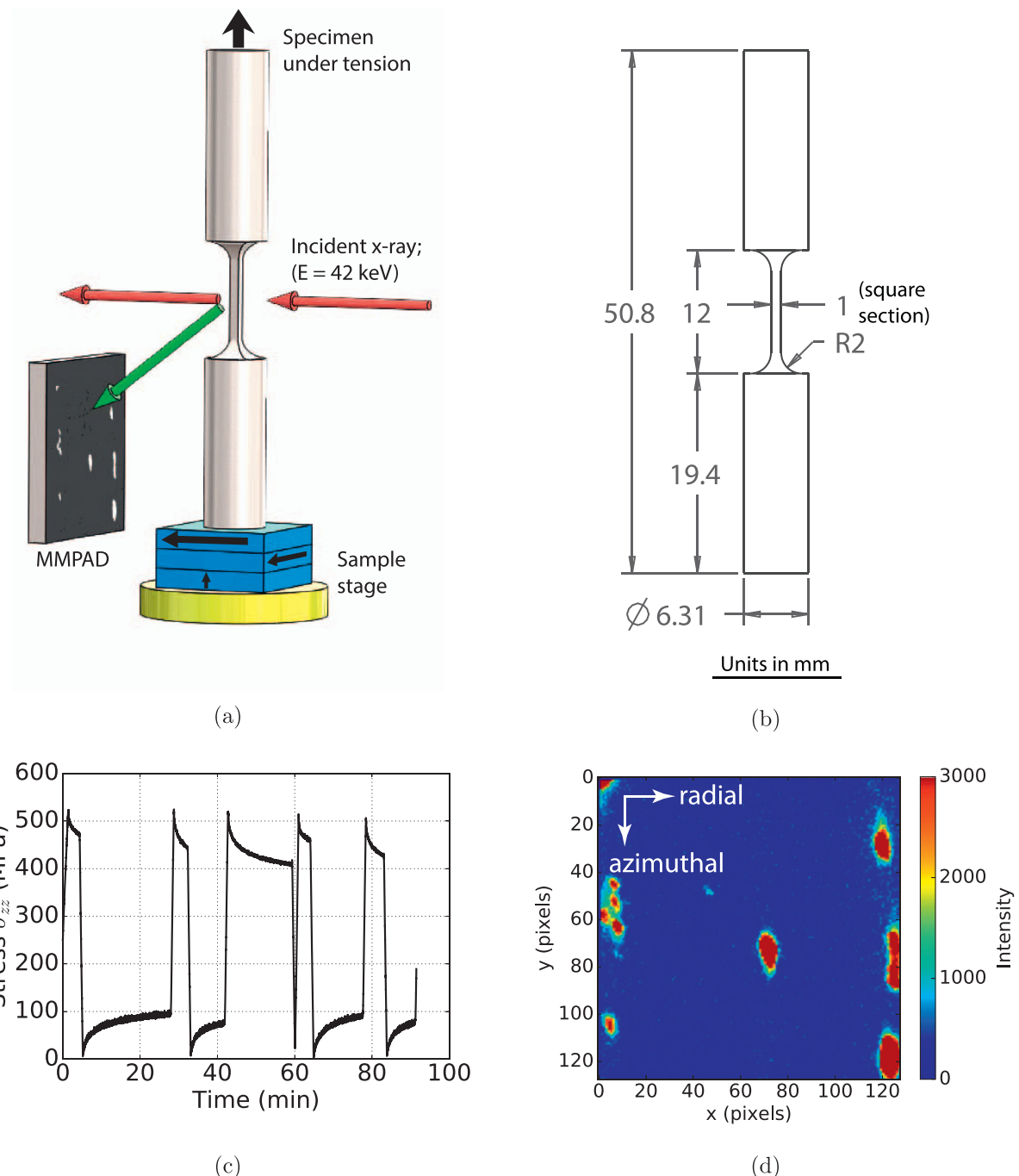


Fig. 2. (a) Schematic of the experimental setup at Cornell High Energy Synchrotron Source. (b) The dimensions of the Ti-7Al sample used in the second set of experiments. (c) Ti-7Al stress relaxation curves. (d) Diffraction spots of Ti-7Al sample collected on the mixed-mode pixel array detector (MM-PAD).

3.2.1. Polycrystal geometry and orientation

Fig. 3 illustrates the method for constructing the meshed polycrystal geometry for finite element simulations. A 3D Voronoi tessellation was created using grain centroid positions as seeds - x and y positions were derived from diffraction image analysis and z positions were the same as the layer height. Neper (Quey et al., 2011), an open-source software, was used to generate the tessellation and also to make a structured mesh for the virtual polycrystal geometry. The meshed geometry was $1.5 \text{ mm} \times 1.5 \text{ mm}$ in cross-section and 0.64 mm in height (Fig. 3), the height being 0.08 mm higher than 0.56 mm range scanned by x-rays for efficacy in generating the tessellation.

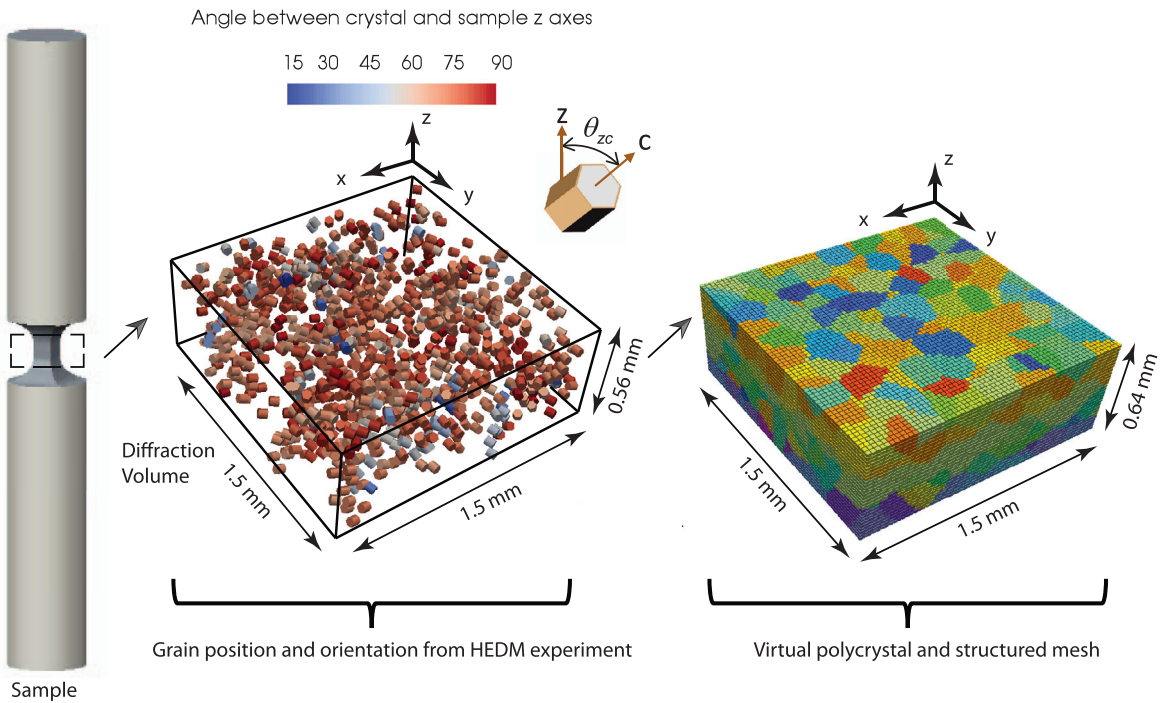


Fig. 3. Scheme for virtual polycrystal and structured mesh generation using experimental data. The hexagonal cylinders represent hcp grains, the cylinders are oriented along the crystal z-axis (c-axis) and colored according the angle between the crystal and sample z-axes, calculated as $\theta_{zc} = \cos^{-1}\left(\frac{\langle z, c \rangle}{\|z\|\|c\|}\right)$.

Table 1
Elastic constants of Ti-7Al alloy (in GPa) (Chatterjee et al., 2016; Venkataraman et al., 2017). See Table 1 of Venkataraman et al. (2017) for the structure Ti-7Al(C).

C_{11}	C_{12}	C_{13}	C_{33}	C_{44}
175.4	80.5	66.8	184.8	46.0

3.2.2. Applied loading

A normal stress (σ_{zz}) was applied on the top surface of the meshed structure for the finite element simulation. The spatial distribution of the applied σ_{zz} was similar to that of the grain-level σ_{zz} obtained from experiments. Grain-level stresses were calculated from the strain using the elastic constants from Table 1. These elastic constants are available from Ref. Chatterjee et al. (2016) and Ref. Venkataraman et al. (2017).

At a lower load i.e. at state B (Fig. 1c) the experimental σ_{zz} distribution represents a pure bending type situation (Fig. 4a) while at a higher load i.e. at state A (Fig. 1c) it represents a tension + bending type situation (Fig. 4b). Therefore the σ_{zz} stresses applied on the model geometry are constructed with similar pure bending and bending + tension trend (Fig. 4c and d). The experimental bending moment can be estimated by integrating the product of the tensile stresses (σ_{zz}) of individual grains with corresponding moment arms (distance of the grain centroids from the neutral axis) over an area covered by the grains under tension in the experimentally-determined pure bending stress state (Fig. 4a). This calculation was performed for the central layer out of the 15 scanned layers. The bending moment was found to be ~ 105 N-mm, where the measured tensile load was 43 N (state B in Fig. 1c). As a point of comparison, the applied bending moment for the simulation, derived in similar fashion from the applied stress state of Fig. 4b, is 109 N-mm.

To account for the presence of initial intergranular residual stresses, the difference between experimental bending stresses developed through fixturing of the sample and those arising from the modeling of the bending deformation associated with this initial loading are used to derive a field of geometrically necessary dislocations (in terms of α) (Fig. 4e) (Appendix A.2). The initial stress state (Fig. 4f) is then rendered using field dislocation mechanics (Roy and Acharya, 2005) (Appendix A.3). For carrying out the simulation,

- first the α field and the pre-existing residual stresses were initialized based on the aforementioned calculations.
- Thereafter, the pure bending type load was exerted on the geometry.

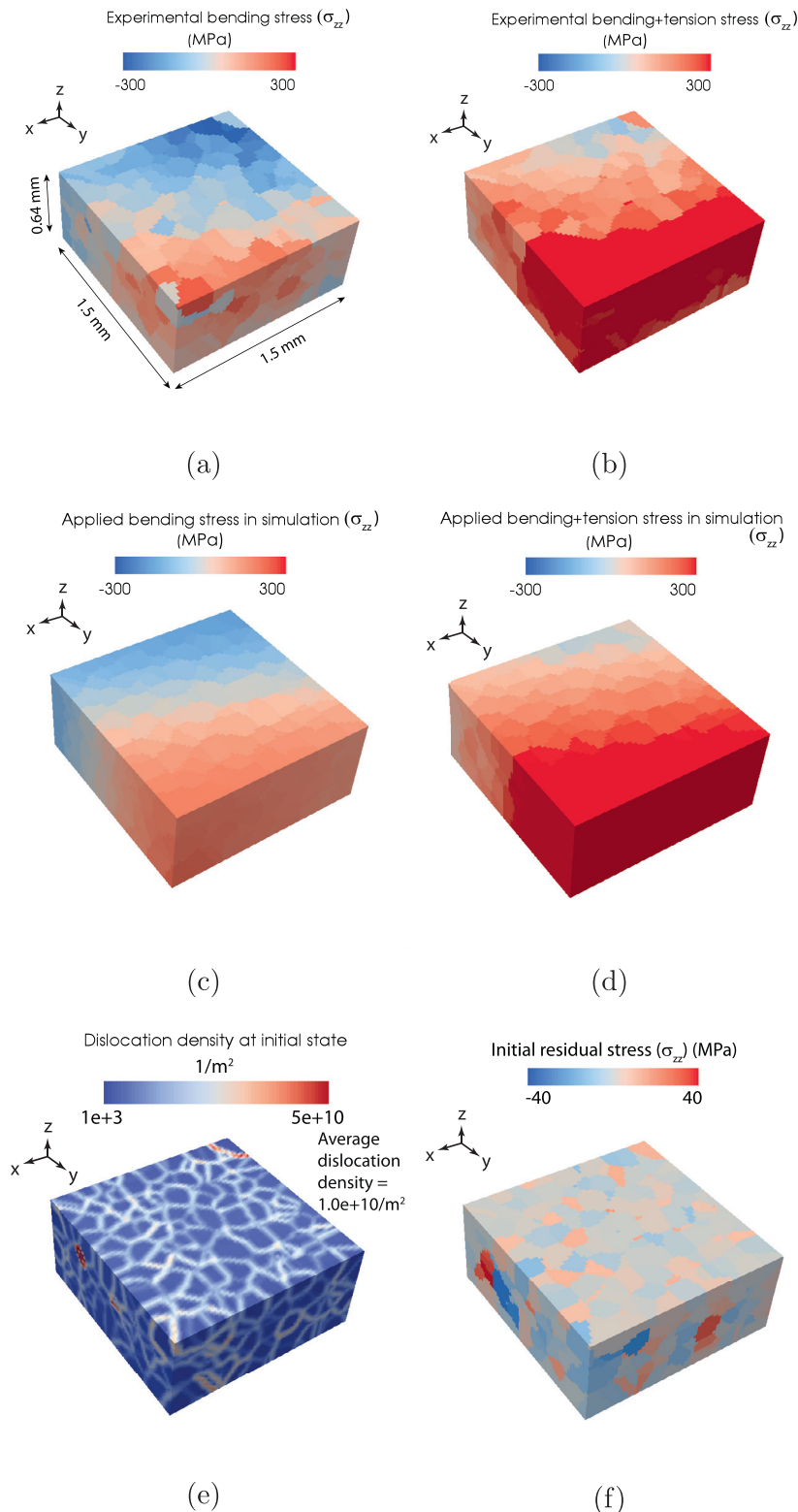


Fig. 4. Pure bending stress state (a) obtained from experiment and (c) applied in simulation. Bending + Tension (b) obtained from experiment and (d) applied in simulation. (e) Initial distribution of dislocation density and (f) Initial residual stress field in simulation.

Table 2

Material parameters used for the RPMFDM based finite element analysis.

Parameter symbol	Parameter name	Parameter value
ρ_m	Mobile dislocation density	$1.0 \times 10^{14} \text{ m}^{-2}$
b	Burgers vector magnitude	$2.9 \times 10^{-10} \text{ m}$
v_0	Reference velocity	$1.7 \times 10^{-6} \text{ m.s}^{-1}$
τ_0	CRSS for prismatic slip system	180.0 MPa (Lütjering and Williams, 2003)
	CRSS for basal slip system	200.0 MPa (Lütjering and Williams, 2003)
m	Strain rate sensitivity for prismatic slip system	0.04 (Section 4)
	Strain rate sensitivity for basal slip system	0.02 (Section 4)
E	Young's modulus x and y	124.4 GPa
E_z	Young's modulus z	158.7 GPa
ν	Poissons ratio x-y plane	0.384
ν_{xz}	Poissons ratio x-z plane	0.289
μ	Shear modulus	50.0 GPa

- After that, the bending + tension load was applied and was held constant for the sample to creep.
- Allowing a period of creep deformation, the sample was subsequently unloaded to obtain the residual stresses.

An assessment of the affect of including the initial residual stress state may be made through application of manifold learning (Appendix B).

3.2.3. Material parameters and slip systems

Prismatic and basal slip systems were used in studying the deformation of hcp Ti-7Al alloy. The critical resolved shear stresses of these two slip systems are significantly lower than that of the pyramidal slip systems at room temperature (Lütjering and Williams, 2003). Therefore prismatic and basal slip systems likely dominate during room-temperature, low stress creep of the alloy. The numerical values of material parameters, used for the modeling, are listed in Table 2. Young's modulus, Poisson's ratio and shear modulus were evaluated from the components of the elastic stiffness matrix (Table 1). Strain rate sensitivities of the prismatic and basal slip systems were derived from a set of high-energy X-ray diffraction data as discussed in Section 3.1 and Section 4.

4. Estimation of strain rate sensitivity

Strain rate sensitivities of the prismatic and basal slip systems of Ti-7Al were calculated by analyzing the stress relaxation data captured by the MM-PAD at a rate of 20 Hz. (Gupta and Li, 1970) formulated the equation for finding strain rate sensitivity from stress relaxation behavior (Eq. (7)).

$$\sigma = \sigma_i + K'(t + a)^{-n} \quad (7)$$

Where σ_i , K' and n are fitting parameters. The strain rate sensitivity (m) can be calculated as follows:

$$\frac{1}{m} = \frac{1}{n} + 1 \quad (8)$$

Tang et al. (2015) re-described Eq. (7) in terms of strain (ε) by dividing the equation with an effective stiffness along a diffraction vector (E_{ref}). For the purpose of the current work, Eq. (9) was derived in a similar way from Eq. (7) to express the stress relaxation in terms of radial shift (Δr) of a diffraction spot. This was possible because $-\Delta r \propto \varepsilon = \frac{\sigma}{E_{ref}}$.

$$-\Delta r = \Delta r_i + K(t + a)^{-n} \quad (9)$$

where $K \propto \frac{K'}{E_{ref}}$. In the present work, diffraction spots were selected from the prismatic ($\bar{2}020$) (Fig. 5a) and pyramidal ($\bar{1}01\bar{3}$) (Fig. 6a) rings. A grain with the diffraction vector in prismatic ($\bar{2}020$) direction has high propensity for prismatic slip and lesser driving force for basal slip. On the other hand, a grain with the diffraction vector in pyramidal ($\bar{1}01\bar{3}$) direction would be oriented more favorably for basal slip. Therefore, for the current work, the strain rate sensitivities calculated from ($\bar{2}020$) and ($\bar{1}01\bar{3}$) spots were considered as representatives of that of the prismatic system and the basal system respectively. Radial intensity distribution peaks were fitted to the spots (Figs. 5b and 6b). The radial shifts of the peaks were plotted with time for the relaxation periods (Figs. 5c and 6c). The strain rate sensitivities were evaluated by fitting Eq. (9) to the time series (Figs. 5c and 6c). Furthermore, the rate of radial shift ($\frac{d\Delta r}{dt}$), when plotted against time should fit to a straight line (at longer times) given by Eq. (10) (Fig. 5c and Fig. 6c).

$$\log\left(\frac{d\Delta r}{dt}\right) = \log(nK) - (n + 1)\log(t) \quad \text{for } t \gg a \quad (10)$$

Strain rate sensitivity relates to slope of the fitted straight line as:

$$\frac{1}{m} = \frac{\text{slope}}{\text{slope} + 1} \quad (11)$$

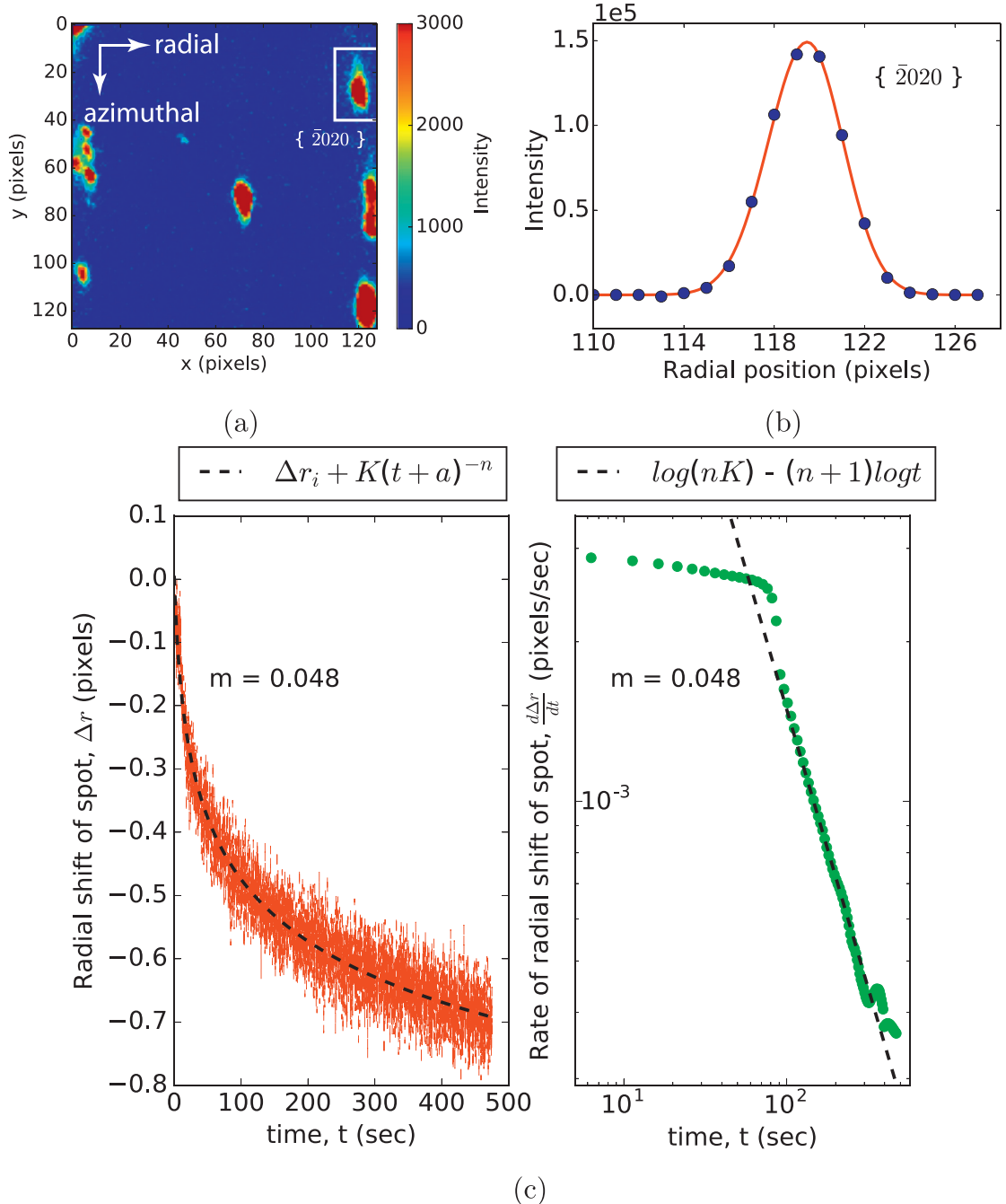


Fig. 5. The plots are for observation no. 1 from Table 3 : (a) Diffraction spot selected from $\bar{2}020$ ring, (b) Radial intensity distribution peak, fitted to the selected spot, (c) Time series of radial shift of peak with fitted curve (Eq. (9)) and rate of radial peak shift with fitted straight line (Eq. (10)).

Strain rate sensitivities of the basal and prismatic slip systems are ~ 0.02 and ~ 0.04 , respectively, as estimated from several stress relaxation observations (Tables 3 and 4). These values follow the trend of rate sensitivities for Ti-6Al-2Sn-4Zr-2Mo alloy obtained by Jun et al. (2016) using their stress relaxation method: these authors give ranges for rate exponents of basal and prism slip as 0.021–0.042 and 0.054–0.063, respectively.

As a simple check for stress relaxation of a polycrystal using the present framework, boundary conditions for uniaxial loading followed by a hold were applied to the realization of Fig. 3. The rate exponent was found to be 0.033, lying between the experimental values for basal and prism slip.

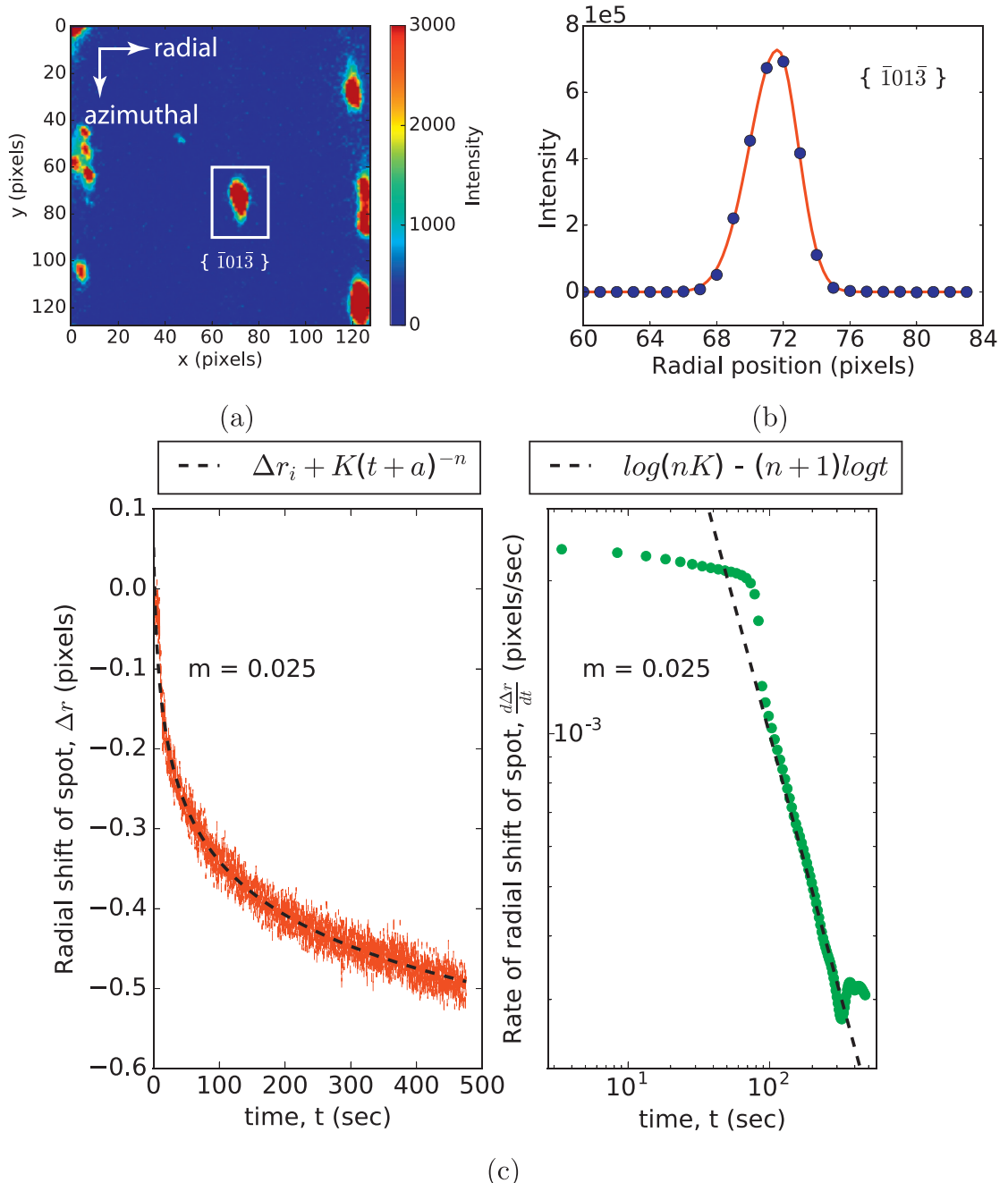


Fig. 6. The plots are for observation no. 1 from Table 4 : (a) Diffraction spot selected from $\bar{1}01\bar{3}$ ring, (b) Radial intensity distribution peak, fitted to the selected spot, (c) Time series of radial shift of peak with fitted curve (Eq. (9)) and rate of radial peak shift with fitted straight line (Eq. (10)).

Table 3
Strain rate sensitivity values obtained from fitting for $\bar{2}020$ spot.

Observation no.	Relaxation starts at stress (MPa)	m
1	530	0.048
2	530	0.038
3	530	0.036
4	530	0.05
5	510	0.034

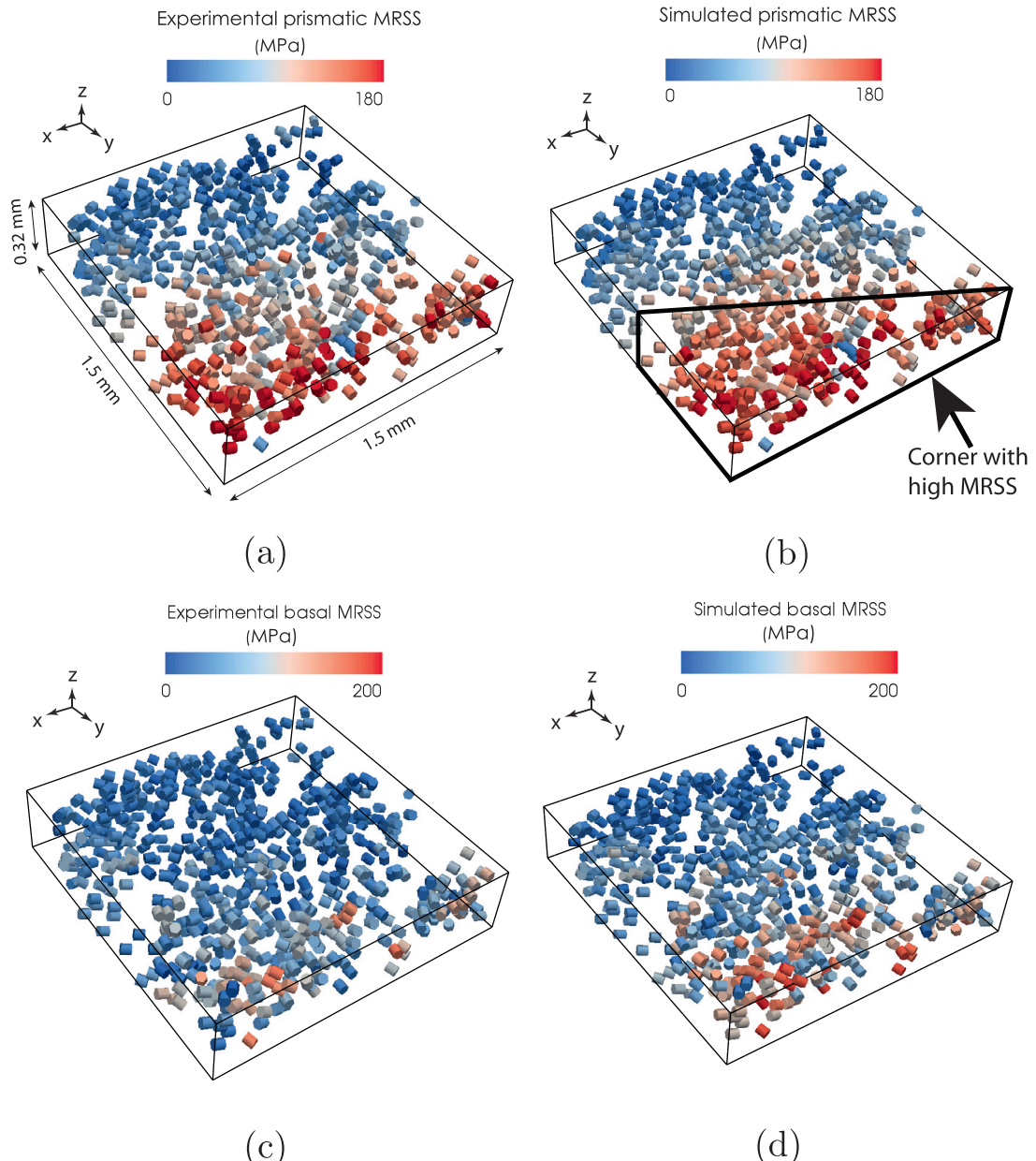


Fig. 7. Comparing the maximum resolved shear stress (MRSS) from experiment and simulation, (a) Experimental prism MRSS, (b) Simulated prism MRSS, (c) Experimental basal MRSS, (d) Simulated basal MRSS.

Table 4
Strain rate sensitivity values obtained from fitting for $\bar{1}0\bar{1}\bar{3}$ spot.

Observation no.	Relaxation starts at stress (MPa)	m
1	530	0.025
2	530	0.026
3	530	0.025
4	530	0.027
5	510	0.020

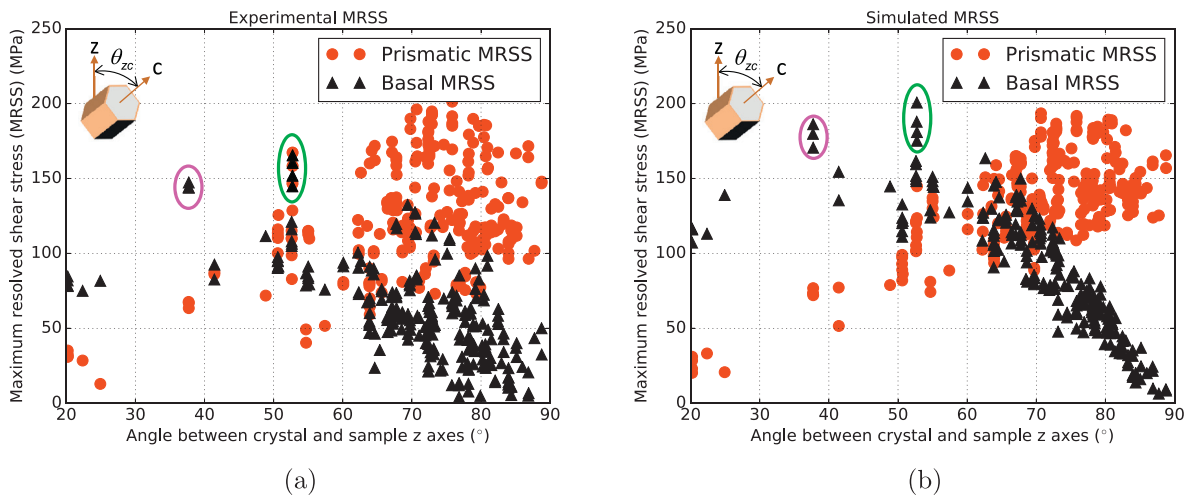


Fig. 8. Trends of (a) experimental and (b) simulated MRSS with angle between crystal and sample z axes, θ_{zc} .

5. Results and discussion

Grain-by-grain distribution of any resultant field is given only for the middle 9 layers out of the 15, the top 3 and the bottom 3 layers are not shown in the following plots. The idea is to explore the grain-level activities away from the boundary (specifically where loading and displacement boundary conditions are applied), in order to avoid any boundary effects.

5.1. Study of slip systems

It was important to compare the slip system activities from experiment and simulation to gain insight into the deformation process. Therefore, we plot the grain-by-grain distribution of maximum resolved shear stress (MRSS), calculated by Eq. (12) from both experimental and simulated data.

$$\tau_{max} = \max_{i,j}(\sigma_{grain} : (\mathbf{s}_i^\alpha \otimes \mathbf{n}_j^\alpha)) \quad (12)$$

In Eq. (12) the following notations are used: α denotes slip system (basal or prism), s_i^α denotes i th slip direction and $n\alpha_j$ denotes j th slip plane normal for α type slip system. Here, σ_{grain} represents the grain-level stress tensor. In Fig. 7a-d, 3D hexagons represent grains, oriented according to their crystallographic orientations. Both the experimental and simulated MRSS distributions indicate a significantly higher prismatic slip system activity compared to basal (Fig. 7a-d). All slip activities are concentrated at the corner where the applied stresses are large (Fig. 7b). Therefore, the grains from that corner are picked and their MRSS values are plotted against the orientation of their crystal z-axis (c-axis) with respect to the sample z-axis (Fig. 8a-b). In Fig. 8a-b, the simulated trends indicate high prismatic MRSS and low basal MRSS at larger orientation angles - these observations agree with the experimental trends. However, the simulated basal MRSS values are overall high (especially in the x-axis range of 40°–60° in Fig. 8b) compared to the experimental ones (Fig. 8a).

The objective was also to understand whether the basal slip system was active, or not. Again, the strain rate sensitivity of basal system is 0.02 (Sections 3.2.3 and 4), which means that the dislocation velocity for basal system would be insignificantly small as long as basal MRSS is less than basal CRSS (200 MPa) and would suddenly rise to a large value thereafter (Eq. (6a)). This large dislocation velocity would help increase the GND density (Eq. (3a)) and hence affect the residual stresses. Thus, the effect of basal slip activity on residual stresses would be prominent for the grains with basal MRSS \geq basal CRSS (200 MPa). In our current work, only a few grains have such high MRSS, as is evident from Fig. 7c-d and the grains with high basal MRSS are marked with green and pink circles in Fig. 8a-b. Residual stress σ_{zz} was investigated for those grains with two different simulations, one using only the prismatic slip system another with both prismatic and basal slip systems. After comparing with experimental residual stresses, it was evident that using only prismatic slip system gives a better correspondence to experiment (Fig. 9b-d) for the grain ensemble in the green circle (Fig. 8a-b) (angles between crystal and sample z axes are $\sim 52^\circ$ as in Fig. 9a). This implies that the basal slip system was probably not active during the mechanical deformation of this ensemble. This conclusion is also endorsed by the fact that the experimentally found basal MRSS values are lower than 200 MPa for all orientations in the grain ensemble. However, the stress distribution for the grain ensemble in the pink circle (Fig. 8a-b) (angles between crystal and sample z axes are $\sim 37^\circ$ as in Fig. 10a), matches better with experiment when both basal and prismatic slip systems are used in simulation (Fig. 10b-d). The variation of basal slip

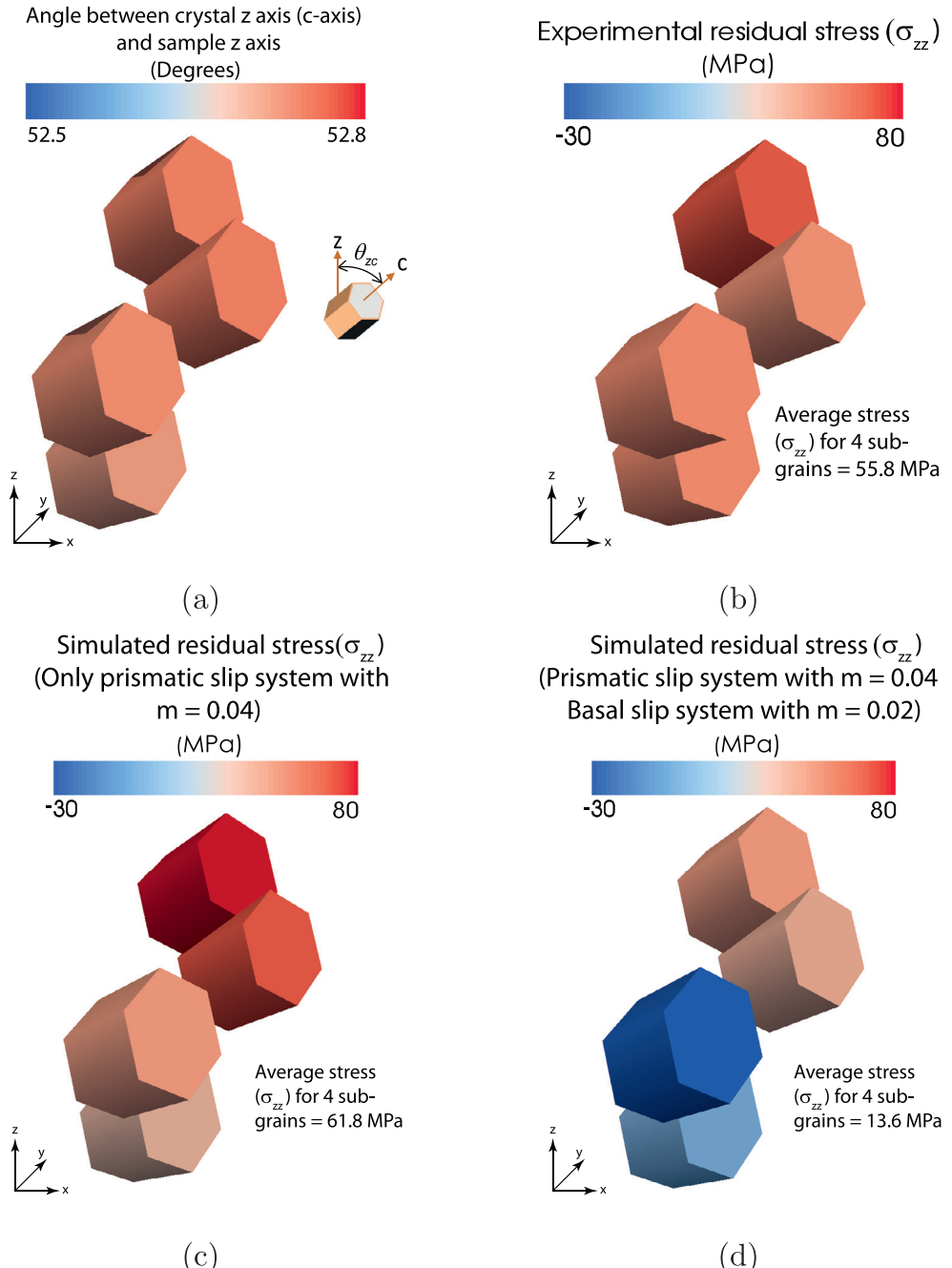


Fig. 9. Characteristics of selected grains with high basal MRSS. (a) Orientations of the grains; the 3D hexagons are oriented along the hcp crystal z-axis (c-axis) and colored according to the angle between the crystal and sample z axes, θ_{zc} . Residual stresses from (b) experiment, (c) simulation with prismatic slip only, (d) simulation with both prismatic and basal slip. Note the comparatively better correspondence between only prismatic and experimental cases.

activity in CP-Ti has been studied recently Wang et al. (2017). While the present study supports the predominance of prism slip, basal slip also plays a role in this alloy.

The grain ensembles in Figs. 9a and 10a, detected from neighboring z layers have nearly identical orientation within the ensemble. Therefore, they represent parts of the same grain – providing a resolution approaching the subgrain scale. Detection of these ‘subgrains’ from several z layers was possible by virtue of the line focused beam (beam height $\sim 2 \mu\text{m}$) used in the experiment, where the average grain size in the sample was $\sim 100 \mu\text{m}$. Figs. 9b-d and 10b-d give the stress gradient inside the respective grain ensembles from experiment and simulation (Fig. 11).

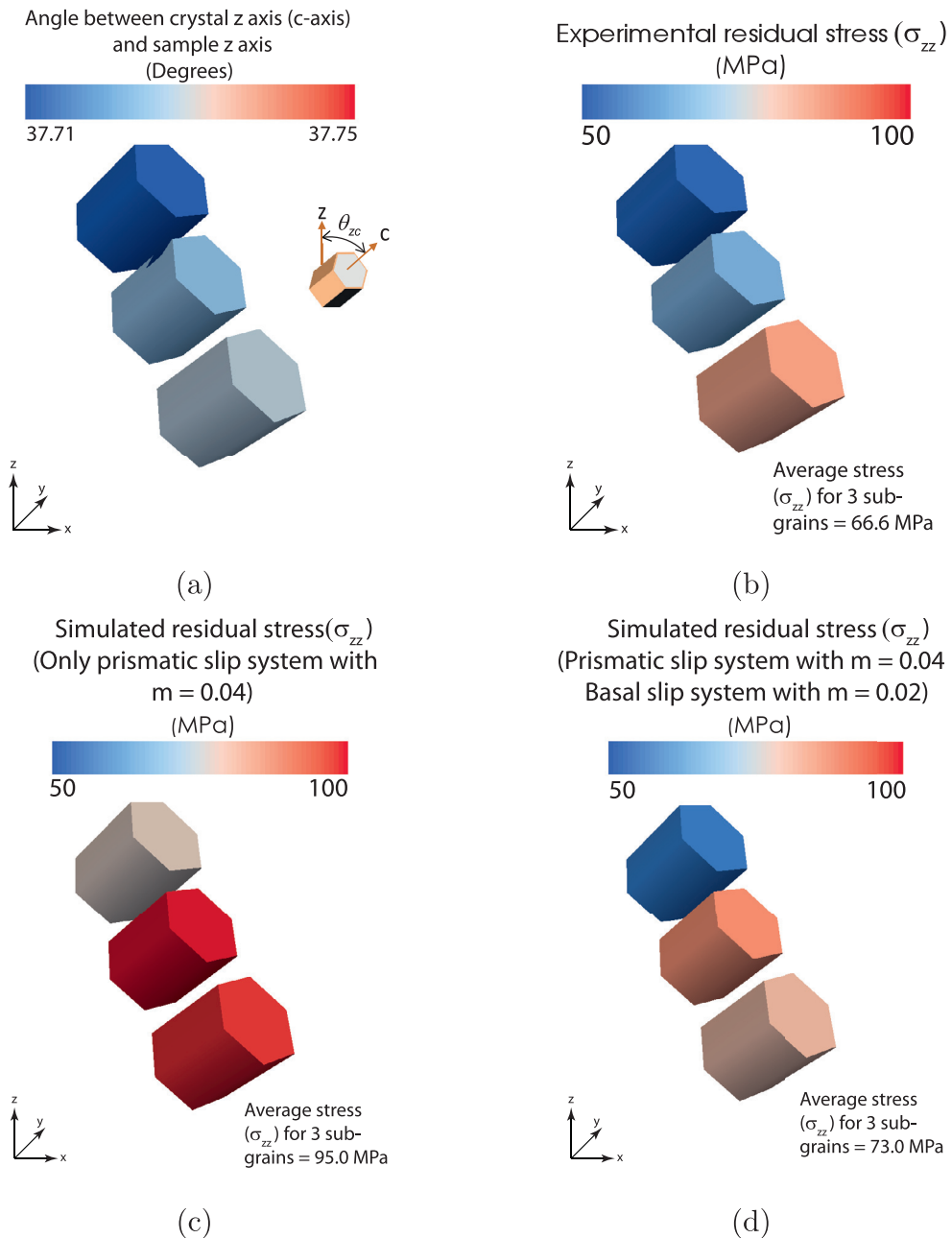


Fig. 10. Characteristics of selected grains with high basal MRSS. (a) Orientations of the grains; the 3D hexagons are oriented along the hcp crystal z -axis (c-axis) and colored according to the angle between the crystal and sample z axes, θ_{zc} . Residual stresses from (b) experiment, (c) simulation with prismatic slip only, (d) simulation with both prismatic and basal slip. Note the comparatively better correspondence between prismatic + basal and experimental cases.

5.2. Residual stress distribution

The discussion advanced in Section 5.1 and Fig. 7a-d indicates that prismatic slip system activity was dominant in the sample during deformation. Simulated grain-by-grain residual stress distributions for the selected middle 9 layers (Fig. 12b) describe that the sample corner with highest prismatic MRSS (highest applied stress) develops significant residual stresses during simulation. This is also evident from the dislocation density distribution plot (Fig. 12c), note that the average dislocation density as in Fig. 12c is about four times that of the initial state as in Fig. 4e. However, the magnitude of simulated σ_{zz} stresses are smaller compared to the experimental ones (Fig. 12a-b). In order to relate the prismatic slip system activity

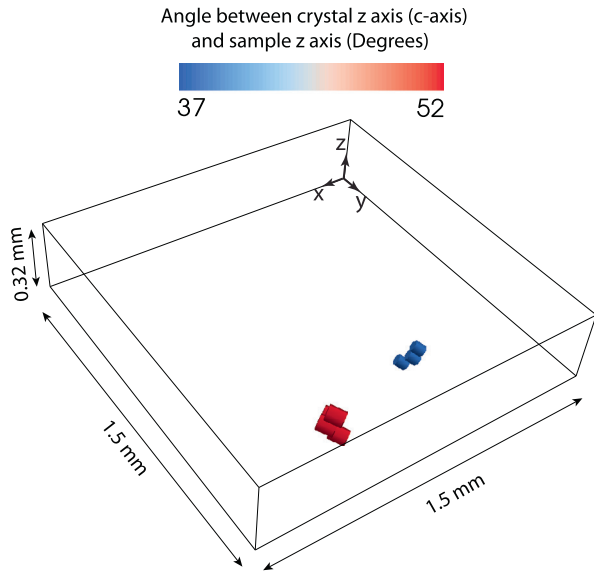


Fig. 11. Location of selected grain groups in the geometry (showing total geometry for 9 layers).

with residual stresses, experimental and theoretical residual stresses are plotted against the angle between the crystal z-axis and sample z-axis for the grains from the most-stressed corner (Fig. 12b) of the sample (Fig. 13a-d). Stress component σ_{zz} decreases (Fig. 13a-b), while σ_{xx} exhibits a slight increase (Fig. 13c-d) with crystal z-axis orientation angle. This behavior is evident from both experiments and simulation (Fig. 13a-d). The grains with higher orientation angles have higher prismatic MRSS (Fig. 8a-b) and they possibly experience permanent tensile deformation (i.e. elongation) in z direction and consequent reduction in dimension in x and y directions. During unloading, these highly deformed grains are constrained by neighboring grains so as to maintain compatibility. A compressive stress component, σ_{zz} , and tensile stress component, σ_{xx} , develop as a consequence. On the other hand, σ_{yy} stresses average out to zero (Fig. 13e-f).

At places other than the most plastically deformed corner, the residual stresses found experimentally likely follow from the initial processing of the material prior to loading the sample (Fig. 12a) (Pokharel and Lebensohn, 2017; Turner et al., 2017). This is somewhat captured in the simulation as an effect of initialization of residual stress field with initial α (Fig. 12b), however, the magnitude of this modeled initial residual stress is less than that found in experiment. [As mentioned above, we pursued a manifold learning technique (Appendix B.1) to qualitatively compare the experimental and simulated residual stresses over the entire 3D volume and hence, point out the importance of initializing the stress field in the current work.] The limitations of using the far-field diffraction data to develop the model will be further addressed in the discussion, below.

6. Conclusions

Grain-level and subgrain-level residual stresses were predicted using a modified field dislocation mechanics based model for Ti-7Al alloy. High energy X-ray diffraction experiments were used to characterize the grain orientations and positions, important for making the 3D simulation geometry. Experimentally found residual stresses, for individual grains and subgrains, were used for validating the modeling results. The strain rate sensitivities of the prismatic and basal slip systems were calculated to be 0.04 and 0.02, respectively, from HEXD experiments. These values were used as input in the modeling. The important conclusions from the work are as follows:

- A majority of the grains deform under prismatic slip activities. The grains oriented at a near 90° angle with the sample z axis experience the highest prismatic resolved shear stress. These grains tend to develop a compressive σ_{zz} stress and tensile σ_{xx} stress in the unloaded state. These trends are observed in both experiments and simulations.
- In the simulations, residual stresses mainly concentrate at the most plastically deformed corner of the geometry. However, in the experiments, residual stresses of similar magnitude prevail all over the geometry which is possibly an outcome of any initial material processing. Initialization of α field, in this simulation, partially captures the effect of any initial residual stresses in the material. Prescription of the initial stress state is a current, and needed, direction for research (Pokharel and Lebensohn, 2017).
- Using a prismatic rate sensitivity of 0.04, as calculated from the HEXD experiments, we get a reasonable correspondence between simulated and experimentally determined residual stresses for grains from the most-stressed corner. However,

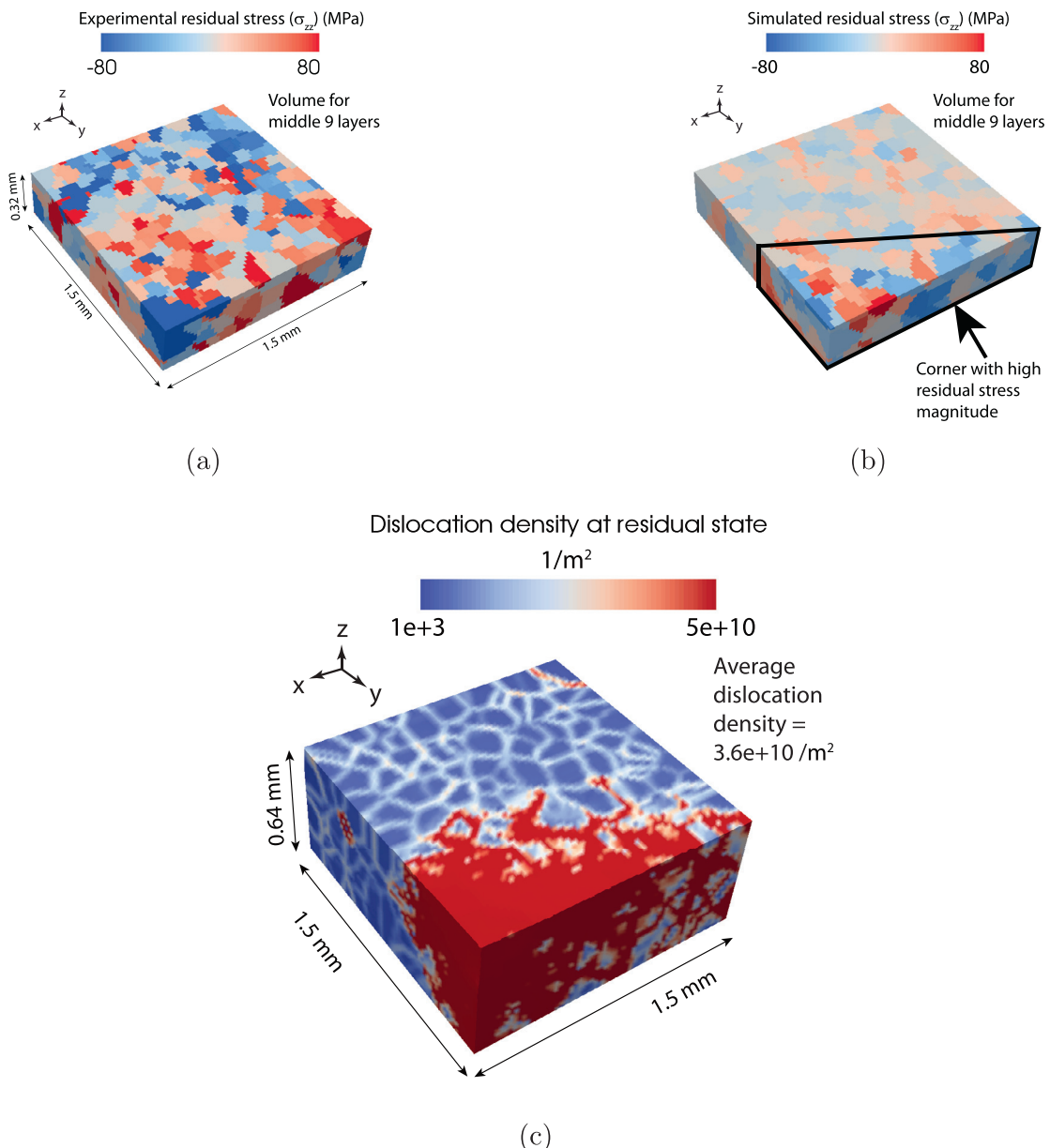


Fig. 12. Grain-by-grain residual stress distribution from (a) experiment and (b) simulation with both prismatic and basal slip. (c) Distribution of dislocation density at the end of the simulation i.e. at the unloaded state.

the limitations inherent in an approximation to the microstructure derived from tessellation about grain center-of-mass positions within measurement slices must be recognized.

- Stress gradients within individual grains are shown to be related to slip system activity.

When considering the above results relating to slip system activity and presence of the initial residual stress, it is important to note the limitations of the far-field diffraction analysis. This technique does not resolve the morphology of individual grains; gradients are rendered only by virtue of translation of the line focus beam along the tensile direction of the sample. This limits the ability to model an initial residual stress state, in equilibrium, that is truly representative of experiment. Further, an exact agreement of intragranular stress gradients, Figs. 9 and 10, is not expected. Complementing combining near- and far-field techniques offers a path for instantiation of grain morphology in a model (Turner et al., 2017). Still, the advancing capability to resolve lattice strain both spatially and temporally, illustrated in the present work, offers another tool for model development and validation.

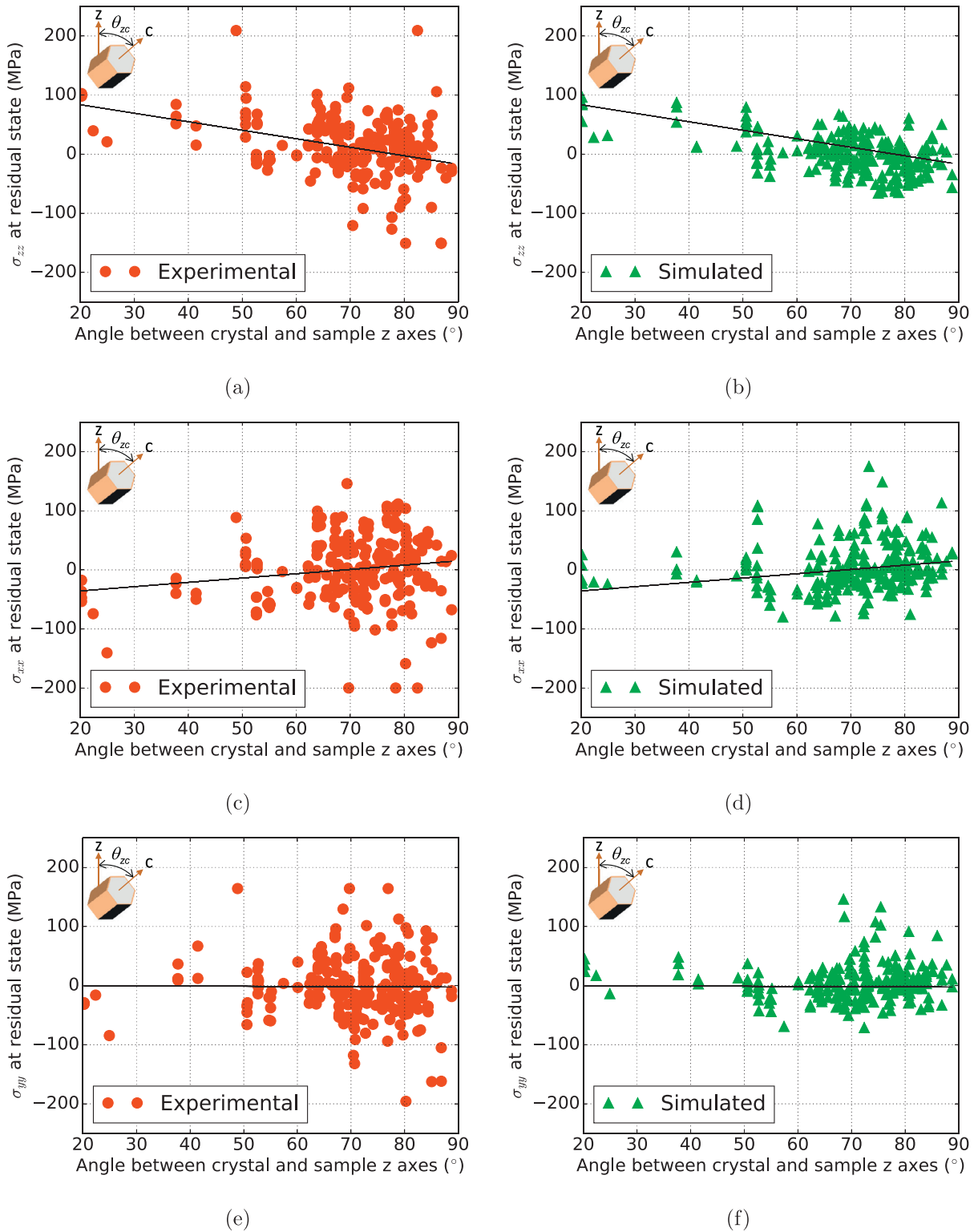


Fig. 13. Comparing the trends of experimental and simulated residual stresses with angle of inclination of crystal z axes(c-axes) with respect to sample z axes, θ_{zc} for (a) σ_{zz} stress, (b) σ_{xx} stress, (c) σ_{yy} stress.

Acknowledgments

A. Beaudoin and K. Chatterjee are supported by the Air Force Office of Scientific Research under Contract No. FA9550-14-1-0369. The use of Advance Photon Source is granted by the US Department of Energy, Office of Science, Office of Basic Energy Sciences under Contract No. DE-AC02-06CH11357. This work is based upon research conducted at the Cornell High Energy Synchrotron Source (CHESS) which is supported by the [National Science Foundation](#) and the [National Institutes of Health/National Institute of General Medical Sciences](#) under NSF award [DMR-1332208](#). MM-Pad detector development is supported by CHESS and [DOE](#) grant [DESC0016035](#). We are indebted to Dr. Paul Shade for providing the Ti-7Al samples used in the experimental study. We wish to thank Prof. Amit Acharya (Carnegie Mellon University) for comments on the manuscript and Mr. Daniel Banco (Tufts University) for introducing us to the method of manifold learning with python. We also want to thank Mr. Kenneth E. Swartz (University of Illinois at Urbana-Champaign), Mr. Daniel Banco (Tufts University), Mr. Mark Obstalecki (Cornell University), Mr. Timothy Long (Cornell University) and Mr. Christopher Budrow (Cornell University) for helping us during the experimentation at CHESS.

Appendix A

A1. Calculation of dislocation velocity \mathbf{V} and effective plastic strain rate in RPMFDM

The dislocation velocity field is determined by [Eqs. \(A.1a\)–\(A.1d\)](#) considering positive dissipation and pressure independence of plasticity ([Acharya and Roy, 2006](#)).

$$\mathbf{V} = \bar{v} \frac{\mathbf{d}}{|\mathbf{d}|} \quad \bar{v} \geq 0 \quad (\text{A.1a})$$

$$\mathbf{d} = \mathbf{b} - \left(\mathbf{b} \cdot \frac{\mathbf{a}}{|\mathbf{a}|} \right) \frac{\mathbf{a}}{|\mathbf{a}|} \quad (\text{A.1b})$$

$$b_i = \varepsilon_{ijk} \sigma'_{jr} \alpha_{rk} \quad (\text{A.1c})$$

$$a_i = \varepsilon_{ijk} \frac{1}{2} \sigma_{mm} \alpha_{jk} \quad (\text{A.1d})$$

where \bar{v} , the magnitude of the velocity vector is obtained from the crystal plasticity formulations. The dislocation velocity magnitude \bar{v} is calculated as an average of absolute value of velocities of all slip systems ([Eq. \(A.2\)](#)) and is used to determine \mathbf{V} ([Eq. \(A.1a\)](#)).

$$\bar{v} = \frac{1}{n_c} \sum_s |\mathbf{v}_s| \quad (\text{A.2})$$

In [Eq. \(A.2\)](#) n_c is the total number of slip systems and v_s , the dislocation velocity of a single slip system is calculated from [Eq. \(6a\)](#). The effective plastic strain rate due to both SSD and GND is determined by [Eq. \(A.3\)](#).

$$\dot{\Gamma} = |\boldsymbol{\alpha} \times \mathbf{V}|_F + \sum_s \rho_m b |\mathbf{v}_s| \quad (\text{A.3})$$

where $|\mathbf{A}|_F$ stands for $\sqrt{\sum_{i=1}^3 \sum_{j=1}^3 A_{ij} A_{ij}}$. Note that there is an interplay between the transport of GND, $\boldsymbol{\alpha} \times \mathbf{V}$, and SSD, ρ_m .

Though not exploited in the present work, evolution of the statistical mobile density offers a means of addressing short-term transients slip system response.

A2. Initialization of dislocation density tensor ($\boldsymbol{\alpha}$)

All the calculations for finding the initial distribution of dislocation density tensor ($\boldsymbol{\alpha}$), were performed at the pure bending state represented by [Fig. 4a](#) and c. Experimentally found grain-level strain tensors, at pure bending state ([Fig. 4a](#)), were assigned to their corresponding elements. Strain values at the element centers were converted to nodal values by simply averaging the contributions of neighboring elements. A similar treatment was done to the simulated strain tensors ([Fig. 4c](#)) at pure bending state. However, here, the stresses for individual elements were found as a simulation output and they were converted to strains using [Eqs. \(A.4a\)–\(A.4c\)](#).

$$[\sigma]_{\text{crystal}} = [U][\sigma]_{\text{sample}}[U]^T \quad (\text{A.4a})$$

$$\{\varepsilon\} = [C]^{-1} \{\sigma\}_{\text{crystal}} \quad (\text{A.4b})$$

$$[\varepsilon]_{\text{sample}} = [U]^T [\varepsilon]_{\text{crystal}} [U] \quad (\text{A.4c})$$

Here, $\{\sigma\}$ and $\{\epsilon\}$ are stress and strain vectors for individual elements, $[C]$ is the elastic stiffness matrix and $[U]$ gives the orientation of crystal frame with respect to sample frame. After finding the nodal values of strains from both experiment (ϵ_{expt}) and simulation (ϵ_{simu}), for the pure bending state, Eqs. (A.5a)–(A.5b) were used to initialize the dislocation density tensor (α) at each node. The excess strains in the experimental data i.e. $\Delta\epsilon = \epsilon_{expt} - \epsilon_{simu}$ were considered to be an outcome of the initial residual stresses.

$$\Delta\epsilon = \epsilon_{expt} - \epsilon_{simu} \quad (\text{A.5a})$$

$$\alpha^{[0]} = -\text{curl}\Delta\epsilon \quad (\text{A.5b})$$

A3. Determination of initial stress and distortion

Initial stress and distortion fields were calculated from the specified initial dislocation density tensor ($\alpha^{[0]}$). The calculation was done in 4 steps and both elastic and plastic distortions were considered to have an incompatible and a compatible part (Roy and Acharya, 2005).

Step 1: The incompatible part (χ_0) of the initial elastic distortion (U_0^e) was determined using Eqs. (A.6a) – (A.6c).

$$\text{curl}\chi_0 = \alpha^{[0]} \quad (\text{A.6a})$$

$$\text{div}\chi_0 = \mathbf{0} \quad (\text{A.6b})$$

$$\chi_0 \mathbf{n} = \mathbf{0} \quad \text{on } S \quad (\text{A.6c})$$

Here, S is the surface around the body under consideration and \mathbf{n} is the unit normal to S .

Step 2: The compatible part ($\text{grad}\chi_0$) of the elastic distortion (U_0^e) was determined by using Eq. (A.7) along with the stress equilibrium and constitutive relations (Eqs. (1a) – (1b)). The boundary condition was considered as $\mathbf{u} = \mathbf{0}$ over the entire body.

$$U_0^e = \text{grad}\chi_0 + \chi_0 \quad (\text{A.7})$$

Step 3: Subsequently, the plastic distortion at the initial state was estimated as $U_0^p = -U_0^e = -(\text{grad}\chi_0 + \chi_0)$.

Step 4: After that, the intial stress field (σ_0) was calculated by invoking Eq. (A.7) in Eq. (1b). Dislocation velocity on particular slip systems and effective plastic strain rate were thereby estimated using Eqs. (6a) and (A.3) respectively.

Appendix B

B1. Two-dimensional manifold learning

Experimental and simulated stress data when represented on two dimensional manifolds, where each point represents the stress history for a single grain, describe very similar manifold structures (Fig. B.14a–c). However, the initialization of dislocation density tensor in the simulation improves the manifold structure and distribution of points in the manifold, showing better agreement with experiment. This indicates that with the incorporation of the initial α , the simulation procedure was improved significantly. The procedure for generating the 2D manifold is described in Eq. (B.1) and we used spectral embedding from scikit-learn (Pedregosa et al., 2011) in python for this purpose.

$$\begin{bmatrix} \sigma_{11}^{b1} & \sigma_{22}^{b1} & \sigma_{33}^{b1} & \sigma_{32}^{b1} & \sigma_{31}^{b1} & \sigma_{12}^{b1} & \dots & \sigma_{11}^{bt1} & \sigma_{22}^{bt1} & \dots & \sigma_{12}^{bt1} & \sigma_{11}^{r1} & \sigma_{22}^{r1} & \dots & \sigma_{12}^{r1} \\ \vdots & \vdots \\ \vdots & \vdots \\ \sigma_{11}^{bn} & \sigma_{22}^{bn} & \sigma_{33}^{bn} & \sigma_{32}^{bn} & \sigma_{31}^{bn} & \sigma_{12}^{bn} & \dots & \sigma_{11}^{bt n} & \sigma_{22}^{bt n} & \dots & \sigma_{12}^{bt n} & \sigma_{11}^{rn} & \sigma_{22}^{rn} & \dots & \sigma_{12}^{rn} \end{bmatrix}_{n \times 18} \xrightarrow{\text{Spectral embedding}} \begin{bmatrix} \text{Dimension1}^1 & \text{Dimension2}^1 \\ \vdots & \vdots \\ \vdots & \vdots \\ \text{Dimension1}^n & \text{Dimension2}^n \end{bmatrix}_{n \times 2} \quad (\text{B.1})$$

In Eq. (B.1) superscript ‘ bm ’ stands for bending in grain number ‘ m ’. Similarly, superscript ‘ btm ’ is bending + tension and ‘ rm ’ is residual stress state in grain number ‘ m ’. Additionally, ‘ n ’ is the total number of grains in the entire simulation geometry.

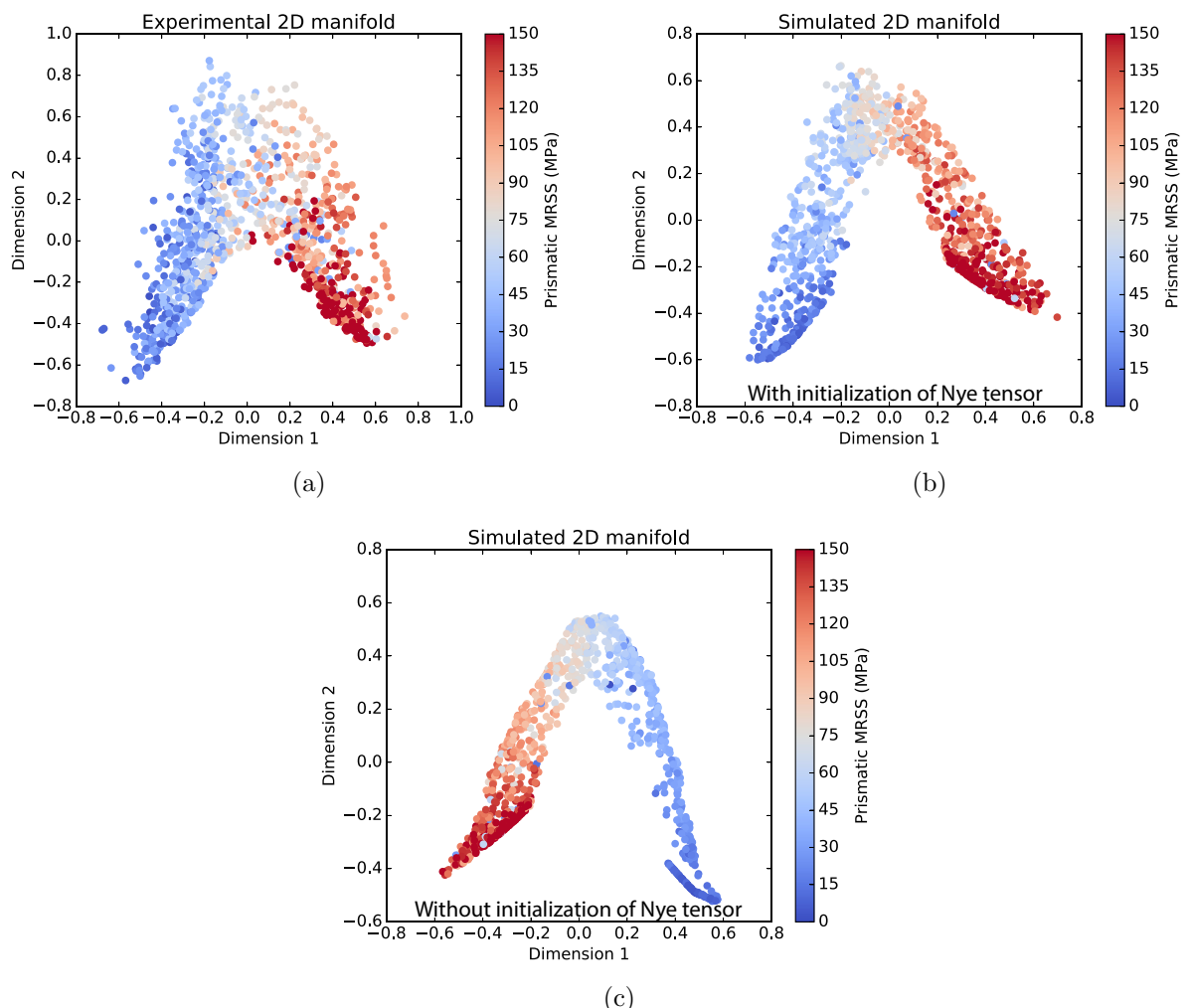


Fig. B.14. Two-dimensional manifold learning with all stress components (procedure described in Eq. (B.1)) from (a) experiment, (b) simulation with initialized dislocation density tensor and (c) simulation without initialized dislocation density tensor.

References

- Acharya, A., 2001. A model of crystal plasticity based on the theory of continuously distributed dislocations. *J. Mech. Phys. Solids* 49 (4), 761–784.
- Acharya, A., Beaudoin, A.J., Miller, R., 2008. New perspectives in plasticity theory: dislocation nucleation, waves, and partial continuity of plastic strain rate. *Math. Mech. Solids* 13 (3–4), 292–315.
- Acharya, A., Roy, A., 2006. Size effects and idealized dislocation microstructure at small scales: predictions of a phenomenological model of mesoscopic field dislocation mechanics: part i. *J. Mech. Phys. Solids* 54 (8), 1687–1710.
- Adenstedt, H.K., 1949. Creep of titanium at room temperature. *Metal Progress* 56 (5), 658–660.
- Arsenlis, A., Parks, D.M., 1999. Crystallographic aspects of geometrically-necessary and statistically-stored dislocation density. *Acta Materialia* 47 (5), 1597–1611.
- Ashby, M.F., 1970. The deformation of plastically non-homogeneous materials. *Philos. Mag.* 21 (170), 399–424.
- Beaudoin, A.J., Obstalecki, M., Storer, R., Tayon, W., Mach, J., Kenesei, P., Lienert, U., 2012. Validation of a crystal plasticity model using high energy diffraction microscopy. *Modell. Simul. Mater. Sci. Eng.* 20 (2), 024006.
- Becker, J., Tate, M.W., Shanks, K.S., Philipp, H.T., Weiss, J.T., Purohit, P., Chamberlain, D., Gruner, S.M., 2017. Sub-Microsecond X-Ray Imaging Using Hole-Collecting Schottky type CdTe with Charge-Integrating Pixel Array Detectors. arXiv preprint [arXiv:1703.02106](https://arxiv.org/abs/1703.02106).
- Becker, J., Tate, M.W., Shanks, K.S., Philipp, H.T., Weiss, J.T., Purohit, P., Chamberlain, D., Ruff, J.P., Gruner, S.M., 2016. Characterization of CdTe sensors with Schottky contacts coupled to charge-integrating pixel array detectors for X-ray science. *J. Instrum.* 11 (12), P12013.
- Bernier, J.V., Barton, N.R., Brandes, M.C., Lienert, U., Miller, M.P., Mills, M.J., 2010. Exploring Crystal Plasticity Via Far-Field 3DXRD. Technical Report. Lawrence Livermore National Laboratory (LLNL), Livermore, CA.
- Chatterjee, K., Venkataraman, A., Garbaciak, T., Rotella, J., Sangid, M.D., Beaudoin, A.J., Kenesei, P., Park, J.-S., Pilchak, A.L., 2016. Study of grain-level deformation and residual stresses in Ti-7Al under combined bending and tension using high energy diffraction microscopy (HEDM). *Int. J. Solids and Struct.* 94, 35–49.
- Dunne, F.P.E., Kiwanuka, R., Wilkinson, A.J., 2012. Crystal plasticity analysis of micro-deformation, lattice rotation and geometrically necessary dislocation density. In: Proc. R. Soc. A, 468. The Royal Society, pp. 2509–2531.
- Dunne, F.P.E., Rugg, D., 2008. On the mechanisms of fatigue facet nucleation in titanium alloys. *Fatigue Fract. Eng. Mater. Struct.* 31 (11), 949–958.

- Dunne, F.P.E., Rugg, D., Walker, A., 2007. Lengthscale-dependent, elastically anisotropic, physically-based hcp crystal plasticity: Application to cold-dwell fatigue in Ti alloys. *Int. J. Plast.* 23 (6), 1061–1083.
- Gupta, I., Li, J.C.M., 1970. Stress relaxation, internal stress and work hardening in LiF and NaCl crystals. *Mater. Sci. Eng.* 6 (1), 20–26.
- FABLE. <http://sourceforge.net/p/fable/wiki/Home/>.
- Hasija, V., Ghosh, S., Mills, M.J., Joseph, D.S., 2003. Deformation and creep modeling in polycrystalline Ti-6Al alloys. *Acta Materialia* 51 (15), 4533–4549.
- Jun, T.-S., Zhang, Z., Sernicola, G., Dunne, F.P.E., Britton, T.B., 2016. Local strain rate sensitivity of single α phase within a dual-phase Ti alloy. *Acta Materialia* 107, 298–309.
- Lütjering, G., Williams, J.C., 2003. Titanium, 2. Springer.
- Messner, M.C., Beaudoin, A.J., Dodds Jr, R.H., 2014. Mesoscopic modeling of crack arrestor delamination in Al-Li: primary crack shielding and T-stress effect. *Int. J. Fract.* 188 (2), 229–249.
- Odegard, B.C., Thompson, A.W., 1974. Low temperature creep of Ti-6Al-4V. *Metall. Trans.* 5 (5), 1207–1213.
- Pagan, D.C., Shade, P.A., Barton, N.R., Park, J.-S., Kenesei, P., Menasche, D.B., Bernier, J.V., 2017. Modeling slip system strength evolution in Ti-7Al informed by in-situ grain stress measurements. *Acta Materialia* 128, 406–417.
- Pedregosa, F., Varoquaux, G., Gramfort, A., Michel, V., Thirion, B., Grisel, O., Blondel, M., Prettenhofer, P., Weiss, R., Dubourg, V., Vanderplas, J., Passos, A., Cournapeau, D., Brucher, M., Perrot, M., Duchesnay, E., 2011. Scikit-learn: machine learning in python. *J. Mach. Learn. Res.* 12, 2825–2830.
- Pokharel, R., Lebensohn, R.A., 2017. Instantiation of crystal plasticity simulations for micromechanical modelling with direct input from microstructural data collected at light sources. *Scripta Materialia* 132, 73–77.
- Poulsen, H.F., 2004. Three-Dimensional X-ray Diffraction Microscopy: Mapping Polycrystals and their Dynamics, 205. Springer Science & Business Media.
- Quay, R., Dawson, P., Barbe, F., 2011. Large-scale 3D random polycrystals for the finite element method: generation, meshing and remeshing. *Comput. Methods Appl. Mech. Eng.* 200 (17), 1729–1745.
- Roy, A., Acharya, A., 2005. Finite element approximation of field dislocation mechanics. *J. Mech. Phys. Solids* 53 (1), 143–170.
- Roy, A., Puri, S., Acharya, A., 2006. Phenomenological mesoscopic field dislocation mechanics, lower-order gradient plasticity, and transport of mean excess dislocation density. *Modell. Simul. Mater. Sci. Eng.* 15 (1), S167.
- Rugg, D., Dixon, M., Dunne, F.P.E., 2007. Effective structural unit size in titanium alloys. *J. Strain Anal. Eng. Des.* 42 (4), 269–279.
- Schmidt, S., 2014. Grainspotter: a fast and robust polycrystalline indexing algorithm. *J. Appl. Crystallogr.* 47 (1), 276–284.
- Shastri, S.D., Almer, J., Ribbing, C., Cederström, B., 2007. High-energy X-ray optics with silicon saw-tooth refractive lenses. *J. Synchrotron Radiat.* 14 (2), 204–211.
- Tang, W., Halm, K.L., Trinkle, D.R., Koker, M.K.A., Lienert, U., Kenesei, P., Beaudoin, A.J., 2015. A study of stress relaxation in AZ31 using high-energy X-ray diffraction. *Acta Materialia* 101, 71–79.
- Tate, M.W., Chamberlain, D., Green, K.S., Philipp, H.T., Purohit, P., Strohman, C., Gruner, S.M., 2013. A medium-format, mixed-mode pixel array detector for kilohertz X-ray imaging. In: *Journal of Physics: Conference Series*, 425. IOP Publishing, p. 062004.
- Taupin, V., Chevy, J., Fressengeas, C., 2016. Effects of grain-to-grain interactions on shear strain localization in al-cu-li rolled sheets. *Int. J. Solids Struct.* 99, 71–81.
- Turner, T.J., Shade, P.A., Bernier, J.V., Li, S.F., Schuren, J.C., Kenesei, P., Suter, R.M., Almer, J., 2017. Crystal plasticity model validation using combined high-Energy diffraction microscopy data for a Ti-7Al specimen. *Metall. Mater. Trans. A* 48 (2), 627–647.
- Varadhan, S.N., 2007. Modeling collective behavior of dislocations in crystalline materials. ProQuest.
- Venkataraman, A., Shade, P.A., Adebisi, R., Sathish, S., Pilchak, A.L., Viswanathan, G.B., Brandes, M.C., Mills, M.J., Sangid, M.D., 2017. Study of structure and deformation pathways in Ti-7Al using atomistic simulations, experiments, and characterization. *Metall. Mater. Trans. A* 48 (5), 1–15.
- Venkatramani, G., Ghosh, S., Mills, M.J., 2007. A size-dependent crystal plasticity finite-element model for creep and load shedding in polycrystalline titanium alloys. *Acta Materialia* 55 (11), 3971–3986.
- Wang, L., Barabash, R.I., Yang, Y., Bieler, T.R., Crimp, M.A., Eisenlohr, P., Liu, W., Ice, G.E., 2011. Experimental characterization and crystal plasticity modeling of heterogeneous deformation in polycrystalline α -Ti. *Metall. Mater. Trans. A* 42 (3), 626–635.
- Wang, L., Zhang, Z., Phukan, H., Kenesei, P., Park, J.-S., Lind, J., Suter, R.M., Bieler, T.R., 2017. Direct measurement of critical resolved shear stress of prismatic and basal slip in polycrystalline Ti using high energy X-ray diffraction microscopy. *Acta Materialia* 132, 598–610.
- Zhang, Z., Jun, T.-S., Britton, T.B., Dunne, F.P.E., 2016. Determination of ti-6242 α and β slip properties using micro-pillar test and computational crystal plasticity. *J. Mech. Phys. Solids* 95, 393–410.
- Zhang, Z., Jun, T.-S., Britton, T.B., Dunne, F.P.E., 2016. Intrinsic anisotropy of strain rate sensitivity in single crystal alpha titanium. *Acta Materialia* 118, 317–330.